CO 2 Solubility in Kimberlite melts CO 2 Solubility in Kimberlite melts

Yves Moussallam, Yann Morizet, Malcolm Massuyeau, Mickaël Laumonier, Fabrice Gaillard

CO_2 Solubility in Kimberlite melts

Yves Moussallam[1], Yann Morizet[1,2], Malcolm massuyeau[1], Mickael Laumonier[1,3], Fabrice Gaillard[1]

[1]ISTO, 7327 Université d'Orléans-CNRS-BRGM, 1A rue de la Férollerie, 45071 Orléans cedex 2, France

[2] Université de Nantes, Nantes Atlantique Universités, Laboratoire de Planétologie et Géodynamique de Nantes (LPGN) UMR CNRS 6112

[3]Bayerisches Geoinstitut, University of Bayreuth, 95440 Bayreuth, Germany

Corresponding author: Yves Moussallam: yves.moussallam@cnrs-orleans.fr

ABSTRACT

Carbon dioxide is the most abundant volatile in kimberlite melts and its solubility exerts a prime influence on the melt structure, buoyancy, transport rate and hence eruption dynamics. The actual primary composition of kimberlite magma is the matter of some debate but the solubility of CO_2 in kimberlitic melts is also poorly constrained due to difficulties in quenching these compositions to a glass that retains the equilibrium CO_2 content. In this study we used a range of synthetic, melt compositions with broadly kimberlitic to carbonatitic characteristics which can, under certain conditions, be quenched fast enough to produce a glass. These materials are used to determine the CO_2 solubility as a function of chemical composition and pressure (0.05-1.5 GPa). Our results suggest that the solubility of CO_2 decreases steadily with increasing amount of network forming cations from ~30 wt% CO_2 at 12 wt% SiO_2 down to ~3 wt% CO_2 at 40 wt% SiO_2 . For low silica melts, CO_2 solubility correlates non-linearly with pressure showing a sudden increase from 0.1 to 100 MPa and a smooth increase for pressure >100 MPa. This peculiar pressure-solubility relationship in low silica melts implies that CO_2 degassing must mostly occur within the last 3 km of ascent to

the surface having potential links with the highly explosive nature of kimberlite magmas and some of the geo-morphological features of their root zone. We present an empirical CO_2 solubility model covering a large range of melt composition from 11 to 55 wt% SiO_2 spanning the transition from carbonatitic to kimberlitic at pressures from 1500 to 50 MPa.

Keywords: kimberlite; carbonatite; CO_2 solubility; transitional melt

1. INTRODUCTION

Experimental investigation of the solubility of CO_2 in kimberlite melt has been limited due to the difficulty in quenching such melt fast enough to form a pure glass (e.g. Brey and Ryabchikov, 1994). Previous studies have therefore estimated the CO_2 solubility based on: (i) extrapolation from trend defined in silicate melts (Brooker et al., 2001) (ii) solubility of melt in partially to highly crystallised experiments (Brooker et al., 2011) (iii) solubility at 0.1 MPa of simple, four components, synthetic compositions considered as analogue to the natural system (Russell et al., 2012) (iv) molecular dynamics simulation studies (Guillot and Sator, 2011). While these studies all suggest that the solubility of CO_2 decreases as the melt becomes enriched in silica, the effect of pressure has remained speculative. Our current knowledge from experimental studies on silicate melt suggests that CO_2 solubility increases with pressure (Blank and Brooker, 1994; Iacono-Marziano et al., 2012; Morizet et al., 2002, 2014) while in pure carbonate melts, CO_2 solubility is more related to satisfying stoichiometric requirements and therefore less dependent on pressure as exemplified by Oldoinyo Lengai's alkali carbonatite lava (Kervyn et al., 2008). However, experiments from Wyllie (1989) and Brooker & Kjardgaard (2011) suggest that there is some 'excess' CO_2 solubility in pure $CaCO_3$ melt, apparently causing a decrease in liquidus temperature.

The composition of primary kimberlite melts in term of volatile and major element chemistry is poorly constrained. Not only are natural kimberlite laden with xenolith and xenocryst

(Mitchell, 2008), but the strong alteration by external fluids they typically endured, in particular serpentinization, strongly affects the volatile and major element composition (Brooker et al., 2011; Sparks et al., 2009). Latest attempt to back-calculate the kimberlite melts chemistry by removal of the serpentinization process points towards an original melt being richer in CO_2 and CaO and poorer in SiO_2, water and MgO than calculated from "uncontaminated" kimberlites (Brooker et al., 2011; Sparks et al., 2009). This findings are corroborated with the fact that the Mg number in kimberlite is too high for equilibrium with a mantle sources (Kopylova et al., 2007; Price et al., 2000) and that liquidus temperature for "uncontaminated" kimberlite composition of 1400°C (Brooker et al., 2011) are higher than predicted from mineral thermometry (Fedortchouk et al., 2002). We therefore chose here to follow from the work of Brooker et al (2011) who argued that kimberlite melts are originally transitional, that is, they have a composition intermediate between a carbonate and a silicate liquid, and investigated several melt compositions with SiO_2 contents between 11 and 32 wt%.

In this contribution, we present results on the first experimental kimberlitic glasses synthesised using an internally heated pressure vessel (IHPV) equipped with an optimised quench configuration. We produced a series of melt compositions across the "transitional" melt field (SiO_2 ~18 to ~32 wt%) to assess the effect of silica activity on CO_2 solubility. The effect of pressure was then investigated by equilibrating melts of similar composition at different pressures (50 to 1500 MPa).

2. EXPERIMENTAL METHODOLOGY

2.1 Starting material

Starting materials were produced by mixing powders from a natural lamproite from Torre Alfina, Italy (table 1, see Peccerillo et al., 1988) with various amounts of synthetic powders of pure oxides and natural dolomite. In order to ensure homogeneity and remove the volatiles present in the Torre Alfina rock, it was fused twice in air at 1400°C and quenched to glass. The composition of all mixtures used as starting materials of all experiments is reported in table 1. The melt compositions we have synthesized here are very Ca-rich when compared to the more Mg-rich typical "contamination free" kimberlite (Mitchell, 1986) but later compare our findings to experiments with more Mg-rich composition. Therefore, an underlying supposition of our work is that Mg and Ca cations behave in a similar way with respect to CO_2 solubility in the melt (see Brey et al., 1991 and Brey and Ryabchikov, 1994 for an investigation of the effect of Mg-Ca substitution on CO_2 solubility in kimberlite melts and see discussion section 5). The Al content of the composition presented here might also be considered slightly high by some authors while the Fe content would be considered low. Notwithstanding these differences, the compositions we explored here provide a close analogue to kimberlite melts (in term of NBO/T for instance) for which the true composition remains unknown and debated (see review by Sparks 2013).

2.2 High pressure experiments; internally heated pressure vessels and piston cylinder

To investigate the solubility of CO_2 in transitional melts at crustal pressure, we performed a series of solubility experiments in the pressure range 50 to 350 MPa at relatively constant temperature (1225 to 1270°C) in relatively dry and oxidized conditions ($\log fO_2$= FMQ+3).

We used internally heated pressure vessels at the ISTO-CNRS laboratory in Orléans, which can reach pressures of up to 400 MPa (± 3 MPa) under controlled temperature up to 1300°C (± 2°C). The vessel was pressurised using argon gas as the pressure medium. A two-Mo-winding vertical furnace was used, creating a 5cm isothermal (± 5°C) "hot-spot" zone and controlled by two S-type thermocouples located on both side of the sample.

Experimental charges consisted of anhydrous sample powder (30 to 150 mg) loaded in gold-palladium ($Au_{80}Pd_{20}$) or platinum capsules (2 to 4 cm in length, 2.5 mm inner diameter and 2.9 mm outer diameter). The capsules were welded shut. Although the initial powder mixtures were stored at 120°C, the strongly hydroscopic character of some oxides (in particular MgO, NaO and K_2O) absorbing atmospheric H_2O within the 15 min necessary to load the capsules, made it impossible to obtain fully water-free experimental charges, hence lowering slightly the XCO_2 in the fluid in equilibrium with the melt at P & T. For each experiment, one to three capsules were hanged by a thin Pt wire. The temperature gradient along the "hot-spot" zone, where the capsules were located, was maintained at about 10°C; the hot zone was always on the top end of the sample. This gradient, although inducing an uncertainty in the run temperature, was part of the quench optimisation strategy as it imposed a thermal profile in the furnace that ensures a strong thermal contrast over a small vertical length located directly below the hanged capsule. Rapid quenching was achieved by passing an electrical current to the holding Pt wire so that the sample dropped into the cold, bottom part of the furnace. The cooling rate was estimated to >100-200°C s^{-1} although no precise estimate could be obtained. After each experiment, capsules were weighed (i) before and (ii) after, opening in order to (i) verify that no leakage had occurred, and (ii) determine the amount of gas not incorporated in the glass. Capsules were then opened and a fragment of the charge was embedded in an epoxy resin and polished for SEM and microprobe analyses. We conducted a total of 18 solubility experiments. The strategy was first to produce a complete

isobaric section at 350 MPa, for a range of melt chemistry spanning SiO_2 from 11 to 38 wt% (expressed as nominal starting composition, Table 1). We then explored the effect of pressure on several compositions (between 17 and 38 wt% SiO_2; expressed as nominal starting composition) from 50 to 350 MPa at temperatures of 1225 to 1270°C. While most experiments successfully produced a pure glass (Fig. 1 and Fig.S1), experiments performed at 50 MPa (run number: TA6_1_6 and TA7_1_3), one experiment at 100 MPa (run number: TA10_1_2) and the experiment with lowest SiO_2 (run number TA15_1_1) could not be quenched fast enough and quench crystals were present throughout the experimental charge (these crystals could not be analysed free of the glass component).

A single piston cylinder experiment was performed at 1.5 GPa and 1300°C in a ½ inch piston-cylinder apparatus. Experimental charge consisted of natural anhydrous sample powder (30 mg) loaded in gold-palladium ($Au_{80}Pd_{20}$) capsules (1 cm in length, 2.5 mm inner diameter and 2.9 mm outer diameter). The capsule was introduced in a talc–pyrex–graphite furnace assembly and surrounded by MgO. A B-type thermocouple was located at ~1 mm atop of the capsule and the run temperature should be considered as a minimum value. The quench of the piston cylinder assembly was not fast enough to prevent the pervasive growth of quench crystals (Fig. 1; Fig. S1; experiment TA6_1_5).

3. ANALYTICAL TECHNIQUES

3.1 EMPA

All experimental products were examined by optical microscope and scanning electronic microscope (SEM) to check for the presence of quench crystals (Fig. S1). Electron microprobe analyses (EMPA) were performed on a Cameca SXFive at the ISTO-CNRS laboratory in Orléans. Glasses were analysed using an accelerating voltage of 15 kV, a beam

current of 6 nA and a defocused beam of 10 µm. Na and K were analysed first in order to minimise alkali loss during analysis. The shortfall in the totals for analysed glasses was broadly consistent with the CO_2 content estimated by other techniques, but systematically higher (Fig. S2).

3.2 Micro-Raman

We used an Innova 300-5W Argon ion laser (Coherent©) operating at 514 nm as the light source to produce Raman scattering. Spectra were collected by a Jobin-Yvon Labram spectrometer (focal distance = 300 mm) equipped with a 2400 grooves/mm CCD detector. Analyses were performed in confocal mode (hole= 500 µm, slit = 200µm) and using a x50 Olympus objective reducing the analysed volume size to a few μm^3. Spectra were acquired over the aluminosilicate network and CO_3^{2-} region between 200 and 1350 cm^{-1}. In a few cases spectra were also acquired in the OH region between 2500 and 3900 cm^{-1}. The acquisition time was of 10 x 60 sec and acquisition depth was optimised in order to obtain the highest Raman signal (Mercier et al., 2009). At least three spectra were acquired for each sample. The CO_2 content in the glass was quantify using the calibration method of Morizet et al. (2013), which provided a reproducibility on the CO_2 measurements of ~5% relative, corresponding to an estimated absolute error on the CO_2 measurements less than 1 wt% for the investigated samples.

3.3 Elemental Analyser

We used a Thermo Scientific, Flash 2000, CHNS elemental analyser to measure water (as H) and CO_2 (as C) in all experimental products. About 1 mg of sample was loaded together with 1 mg of vanadium pentoxide in a tin capsule folded and analysed by combustion at 1800°C. The analyser was calibrated directly prior to analysis and reproducibility on external

standards (marble, dolomite and hydrated basalt) was found to be better than 2% for C and 10% for H, giving an estimated error on the CO_2 measurement of < 1 wt%.

3.4 Gravimetric Weight loss

After experiments the capsules were weighed using a high precision balance before and after puncture, to measure the mass of CO_2 (± H_2O) in the excess fluid phase from which, the mass of dissolved CO_2 in the glass can be calculated by mass-balance. The error associated with this technique depends largely on the initial amount of material loaded in the capsule. Considering a maximum error on the weight measurements of 0.5 mg, for a minimum amount of loaded material of 30 mg, the error on the subsequent CO_2 estimate by this method is < 2 wt%. There may also be an under-estimation of fluid phase mass if some is retained in enclosed bubbles. However, most vesicles are found at the capsule wall (see Fig 1); as a result, most of the fluid must be released on piercing.

4. RESULTS

All experimental charges were CO_2 saturated. This was attested by the presence of bubbles in all investigated charges (Fig.1) and by weight loss after piercing the capsules. All results from solubility experiments are reported in Table 2 with CO_2 content estimated from elemental analyser, weight loss (after capsule puncture), EMPA and micro-Raman spectroscopy. A comparison of the four different methods used to measure the CO_2 content of the experimental charges is presented in Fig. S2. This figure shows that the agreement between the Raman, elemental analyser and gravimetric weight loss methods is very good. Estimates from EMPA shortfall are consistently overestimating the amount of CO_2 even after correction for H_2O (determined by elemental analyser), suggesting that using EMPA shortfall to estimate the melt CO_2 content might be inaccurate. Unless stated otherwise, all CO_2

194 contents reported in the following figures are from measurements using the elemental
195 analyser. The results of CO_2 solubility experiments at 350 MPa for a range of compositions
196 are reported in Fig. 2 together with a data point from an earlier study using a similar
197 composition (Iacono-Marziano et al., 2012). Fig.2 clearly shows a decrease in CO_2 solubility
198 with increasing amount of network forming cations (Si^{4+} and Al^{3+}). This decrease appears to
199 be smooth and continuous across the transitional field. The effect of pressure, that is
200 nominally the pressure of CO_2, on solubility is shown in Fig. 3 for starting compositions at 18
201 to 41 wt% SiO_2 (SiO_2 + Al_2O_3 of 21 to 51 wt% respectively, expressed with volatiles at
202 saturation at 350 MPa). Since experiments at 50 MPa could not be quenched fast enough to
203 prevent the growth of quench crystals, CO_2 solubility was estimated from the amount of gas
204 released after capsule puncture and their CO_2 contents are therefore associated with a larger
205 error (estimated at ±2 wt%) than those determined by elemental analyser (estimated at < 1
206 wt%). At 18 wt% SiO_2 (at the edge of the carbonate field) a pressure drop from 1500 to 180
207 MPa seems to have a limited effect on the solubility of CO_2 (25 to 20 wt% CO_2) and most of
208 the solubility drop takes place from 100 to 0.1 MPa (assuming no CO_2 remains in the melt at
209 0.1 MPa). This results in a strongly non-linear dependence of CO_2 solubility with pressure for
210 melt compositions with SiO_2 contents in the range 18-30 wt%. At SiO_2 content higher than 30
211 wt% the solubility dependence on pressure (from 350 to 0.1 MPa) is linear, as expected in
212 silicate melts for the pressure range considered.

213 ## 5. DISCUSSION

214 Evidence for a genetic connection between kimberlite and carbonatite magmas goes beyond
215 their, long noticed, spatial and temporal occurrence (e.g. Janse, 1975; Mitchell, 2005; White
216 et al., 1995). Kimberlite and carbonatite melts can both be produced by very low degree
217 partial melting of a carbonated mantle source as inferred from their high concentration of

incompatible trace elements (Nelson et al., 1988) and from high pressure melting experiments of carbonated peridotite phase assemblages (Dalton and Presnall, 1998; Dasgupta and Hirschmann, 2006; Ghosh et al., 2009; Gudfinnsson and Presnall, 2005; Rohrbach and Schmidt, 2011). In addition kimberlite and carbonatite melts have been argued to be related by fractionation processes (Dalton and Presnall, 1998; Dawson and Hawthorne, 1973; Larsen and Rex, 1992). This clear link between the two types of magma supports the hypothesis of Brooker et al. (2011) that kimberlite primary magmas were originally more transitional or carbonatitic in composition. The set of transitional synthetic super-liquidus melt compositions that have been produced here should therefore yield a robust approximation of the solubility law for CO_2 in primary kimberlitic melts.

5.1 Empirical model of CO_2 solubility in carbonated melts

Based on the solubility experiments presented here and literature data we developed a purely empirical model of CO_2 solubility as a function of the amount of network forming cations (SiO_2 + Al_2O_3) and pressure. We emphasised that it is the first modelling effort addressing such low silica melt compositions. The simple model is defined as a third order polynomial linking the amount of CO_2 dissolved in the melt to the SiO_2 + Al_2O_3 content and in which each coefficient is in turn a function of pressure as follow:

$$CO_{2_{wt\%}} = A \times (SiO_2 + Al_2O_3)^3 + B \times (SiO_2 + Al_2O_3)^2 + C \times (SiO_2 + Al_2O_3) + D \quad \textbf{(1)}$$

Where:

$$A = a \times P^b$$

$$B = c \times P^d$$

$$C = e \times P^f$$

With *D*, *a*, *b*, *c*, *d*, *e* and *f* representing adjusted parameters reported in Table 3. The rationale behind the formulation of equation (1) is to simulate a pressure-dependent process of dilution

from a pure carbonate end-member (D=50) with the addition of network-forming cations (SiO_2 and Al_2O_3). In order to adjust the parameters in equation (1), we used CO_2 solubility data for basalt (Mattey, 1991; Pawley et al., 1992; Shishkina et al., 2010; Stolper and Holloway, 1988), haplo-phonolite (Morizet et al., 2002), phonotephrite (Behrens et al., 2009), melilitite (Brooker et al., 2001) in addition to selected data from Brey and Ryabchikov, (1994); Brooker, (1995); Brooker et al., (2011); Brooker and Kjarsgaard, (2011); Iacono-Marziano et al., (2012); Morizet et al., (2013); Morizet et al., (2014) and this study (all shown in the subsequent figures). Equation (1) reproduces our experimental data well (standard deviation of 0.9 wt% CO_2 between the modelled and measured values) and allow us to explore a larger P-$X_{(SiO2 + Al2O3)}$ space. Fig. 4 shows the modelled solubility of CO_2 as a function of pressure for compositions ranging from SiO_2 + Al_2O_3 of 0 to 51 wt% and pressure from 1500 to 10 MPa. Fig.4 shows the gradual change in the CO_2 solubility behaviour from carbonate to silicate end-member melts as a function of pressure. We note that from Fig.4, a typical transitional melt enters the kimberlite "root zone" (see the classical model from Hawthorne, 1975) with a CO_2 content of 10 to 18 wt%, consistent with the "target value" of 15 wt% determined by Brooker et al. (2011) for kimberlites.

The range of experiments presented here is not extensive enough to incorporate the effect of temperature and alkali content in equation (1). For this, we considered the available from the literature. Fig. 5 compares data from a range of studies and shows the evolution of CO_2 solubility as a function of network forming cations (SiO_2+Al_2O_3) for a large range of composition and pressure from 2000 to 50 MPa. The predicted evolution from equation (1) is also shown for pressure between 2000 and 20 MPa. The melt composition of all data shown in Fig 5 is reported in Table S2, where one can notice the wide range of compositions explored by these various studies. The variety of methods used to estimate the CO_2 content in

these studies (EMP shortfall, Raman, FTIR, elemental analyser and gas chromatography), makes the comparison of dataset not ideal. In addition, while the present study, that of Iacono-Marziano et al., (2012), Morizet et al., (2014), Brooker et al., (2001) and Brey and Ryabchikov, (1994) are from super-liquidus experiments, data from Brooker *et al.,* (2011) are from patches of glass in mostly crystallised charges while data from Brooker and Kjarsgaard (2011) and Brooker (1995) are from silicate melts coexisting with an immiscible carbonate melt. Perhaps most importantly, the CO_2/H_2O ratio varies widely over the reported dataset with volatile component in experiments from Iacono-Marziano et al., (2012) and Morizet et al., (2014) being dominated by H_2O. Keeping in mind these limitations in the comparison, we can see that the set of data from Morizet et al. (2014) at 350 and 100 MPa and Morizet et al. (2013) at 1000 MPa are well reproduced by our model. A similar agreement is noted with the data at 2000 MPa from Brooker et al., (2001), at 200 MPa from Brooker et al (2011) and (to a lesser extent) at 1500 MPa from Brooker (1995). We also note that data at 1000 MPa from Brey and Ryabchikov (1994) (we only report experimental data at 1000 MPa where they reported clear glass) are also well reproduced despite the significant difference in terms of chemical composition (MgO up to 27wt%). Fig 6, shows a plot of experimentally determined vs. calculated CO_2 solubility from which it appears that the highest deviation from the model are for data by Brooker et al (2011) and Brooker and Kjarsgaard (2010). We made several attempt to link the deviation from the modelled value to the melt composition (Na_2O, K_2O, Na_2O+K_2O, SiO_2/Al_2O_3) but could not find any robust correlations. There is however a hint that melt compositions rich in alkali can incorporate more CO_2 than comparatively Ca and Mg-rich compositions (see in Fig. 5 the isolated experiment from Brooker (1995) at 1500 MPa with 15.6 wt% CO_2 and a composition of 0 wt% CaO and 37 wt% Na_2O). As additional experimental data become available, future models should be able to explore the full effect of composition (in term of Mg, Ca, Na, K, Fe cations) on CO_2 solubility.

A strong correlation was found between the method used to determine CO_2 content and deviation from our model value. Indeed, 70% of the data located further than two standard deviations away from their calculated value had CO_2 content determined by shortfall of EMPA analyses. Comparing our own EMPA shortfall measurements to CO_2 determined by bulk analyser (Fig. S2), we observe that determining the CO_2 content by EMPA shortfall can lead to an overestimation of 2 to 6 wt% CO_2. We therefore conclude (i) that most of the literature data yielding CO_2 solubility values that deviates from our model can be attributed to the large error associated with estimating CO_2 content from EMPA shortfall and (ii) that from the current, limited, dataset there is no identifiable systematic deviations related to the melt composition. Equation (1) therefore provides a good first order approximation of the CO_2 content of carbonated melt over a large range of composition (SiO_2 < 55 wt%; Na_2O+K_2O < 22 wt%). The entrapment pressure of recently reported CO_2-rich melt inclusions from Oldoinyo Lengai (de Moor et al., 2013) for instance, can be estimated using equation (1) (yielding an entrapment depth of 265 to 2085 MPa for inclusions containing 3 to 8 wt% CO_2).

5.2 Implications for Kimberlite ascent and volcanism

As hypothesised by Brooker et al (2011) our results indicate that CO_2 solubility decreases with increasing amount of network forming cations over the carbonate-silicate transitional field. This finding supports the conclusions of Russell et al., (2012) that an ascending carbonate melt, assimilating mantle orthopyroxene (OPX) and becoming progressively enriched in silica, will release an increasing amount of CO_2 into the gas phase and promote magma ascent by keeping it buoyant in spite of increasing xenocryst loading. The effect of pressure (shown in Fig. 3 and 4) on transitional melts appears to be a function of their composition; melts with a composition closer to the carbonate end-member retain a large

quantity of CO_2 until very shallow (3 km) depth while slightly more silicate-rich melts show a continuous and progressive degassing profile with CO_2 being equally released from mantle depth to the surface. The solubility-pressure relationships shown by the transitional melt compositions in Fig. 3 and 4 are intermediate between the behaviour of a carbonate melt which will show little pressure dependence on solubility, and that of a typical silicate melt which will show a mostly linear relationship in the pressure range considered (Fig. 3, 4,e.g. Papale et al., 2006; Iacono-Marziano et al 2012).

The behaviour of transitional melts, retaining more than 18 wt% CO_2 up until very shallow depth should lead to a rapid increase in ascent velocity while reaching the last 3 km depth where important quantities of CO_2 will be released (Fig. 4). This acceleration will be exacerbated by the fact that the volume fraction of gas will reach values higher than 77%, corresponding to the point at which the bubble foam will collapse (Woods, 1995) changing the continuous phase from a bubbly liquid magma to an ash-laden gas and therefore considerably increasing the flow speed as the frictional force become much smaller and the viscosity becomes closer to that of the gas phase. This ascent scenario can readily explain some of the typical morphological features of kimberlite pipes. (i) The widening upward geometry of the pipe, typical of eruptions happening at depth, can be explained by the high amount of CO_2 released over a, most probably, very small time increment leading to overpressure and explosion below the surface. (ii) The appearance of breccias and irregularly shaped blocks at depth of ~3 km, in the “root zone” (see the classical model from Hawthorne, 1975) is consistent with large amount of CO_2 starting to be released at this depth and the associated rapid volumetric expansion (Fig. 4). The occurrence of hypabyssal intrusions of kimberlites however suggests that some kimberlite stall during their ascent through the crust. Although we cannot confidently assign a reason for this, possibilities include the loss of

volatiles, segregating from the magma during ascent or the progressive cooling of the magma (Kavanagh and Sparks, 2009), both process inducing crystallisation and greatly increasing magma viscosity. Experiments on these compositions suggest that crystallisation is extremely rapid, as illustrated by the speed at which quench crystals formed in some of our experiments.

While CO_2 is the most abundant volatile in kimberlite magmas, an unknown but probably significant amount of water is also dissolved in these melts (up to 10 wt%; Kopylova et al., 2007; also see discussion in Sparks et al., 2009 and experimental investigation by Keppler, 2003). Water degassing is therefore likely to exert a large influence on the ascent dynamics of Kimberlite melts. It remains unclear however whether this process would enhance, limit or displace the depth at which the CO_2-exsolution-triggered acceleration of kimberlite melts that we predict takes place.

6. CONCLUSIONS

We have determined CO_2 solubility laws for kimberlite melt and have also provided a general solubility model for carbonated melt composition (SiO_2 < 55 wt%) at pressure between 50 and 1500 MPa. We found that (i) CO_2 solubility decreases steadily with increasing amount of network forming cations (ii) The effect of pressure on CO_2 solubility is a strong function of composition with low SiO_2 melts retaining large amount (~15 wt%) of CO_2 up to very shallow pressure (~100 MPa) while more silicated melts have a near linear CO_2 solubility dependence on pressure. We propose that this peculiar pressure-solubility dependency should result in a strong acceleration of an ascending kimberlite magma in the last 3 km of crust where CO_2 starts to exsolve in large quantities. This behaviour can explain morphological features of kimberlite pipes, notably the depth extent of the root zone and the widening-

upward shape of the conduit and can account for the highly explosive character of Kimberlite eruptions.

ACKNOWLEDGEMENTS

We are very grateful to Rémi Champallier and Leïla Hashim for their help with various instruments. Special thanks also go to Ida Di Carlo for help with the electron probe analyses and to Marielle Hatton for help with the elemental analyser. Funding for this work was provided by the European Research Council (ERC grant number 279790) and the Agence Nationale de la Recherche (ANR-10-BLAN-62101). Valuable reviews by K. Russell and R. Brooker improved the quality of the manuscript. We also thanks the guest Editors of this special issue.

REFERENCES

Behrens, H., Misiti, V., Freda, C., Vetere, F., Botcharnikov, R.E., Scarlato, P., 2009. Solubility of H (sub 2) O and CO (sub 2) in ultrapotassic melts at 1200 and 1250 degrees C and pressure from 50 to 500 MPa. Am. Mineral. 94, 105–120. doi:10.2138/am.2009.2796

Blank, J.G., Brooker, R.A., 1994. Experimental studies of carbon dioxide in silicate melts; solubility, speciation, and stable carbon isotope behavior. Rev. Mineral. Geochem. 30, 157–186.

Brey, G.P., Kogarko, L., Ryabchikov, I.., 1991. Carbon dioxide in kimberlitic melts. N Jb Min. Mh H4, 159–168.

Brey, G.., Ryabchikov, I.., 1994. Carbon dioxide in strongly undersaturated melts and origin of kimberlitic magmas. N Jb Min. Mh H10, 449–463.

Brooker, R.A., 1995. Carbonatite genesis; the role of liquid immiscibility to 25 kb (PhD thesis). University of Manchester.

Brooker, R.A., Kjarsgaard, B.A., 2011. Silicate–Carbonate Liquid Immiscibility and Phase Relations in the System SiO2–Na2O–Al2O3–CaO–CO2 at 0·1–2·5 GPa with Applications to Carbonatite Genesis. J. Petrol. 52, 1281–1305. doi:10.1093/petrology/egq081

Brooker, R.A., Sparks, R.S.J., Kavanagh, J.L., Field, M., 2011. The volatile content of hypabyssal kimberlite magmas: some constraints from experiments on natural rock compositions. Bull. Volcanol. 73, 959–981. doi:10.1007/s00445-011-0523-7

Brooker, R.., Kohn, S.., Holloway, J.., McMillan, P.., 2001. Structural controls on the solubility of CO2 in silicate melts: Part I: bulk solubility data. Chem. Geol. 174, 225–239. doi:10.1016/S0009-2541(00)00353-3

Dalton, J.A., Presnall, D.C., 1998. The Continuum of Primary Carbonatitic–Kimberlitic Melt Compositions in Equilibrium with Lherzolite: Data from the System CaO–MgO–Al2O3–SiO2–CO2 at 6 GPa. J. Petrol. 39, 1953–1964. doi:10.1093/petroj/39.11-12.1953

Dasgupta, R., Hirschmann, M.M., 2006. Melting in the Earth's deep upper mantle caused by carbon dioxide. Nature 440, 659–662. doi:10.1038/nature04612

Dawson, J.B., Hawthorne, J.B., 1973. Magmatic sedimentation and carbonatitic differentiation in kimberlite sills at Benfontein, South Africa. J. Geol. Soc. 129, 61–85. doi:10.1144/gsjgs.129.1.0061

De Moor, J.M., Fischer, T.P., King, P.L., Botcharnikov, R.E., Hervig, R.L., Hilton, D.R., Barry, P.H., Mangasini, F., Ramirez, C., 2013. Volatile-rich silicate melts from Oldoinyo Lengai volcano (Tanzania): Implications for carbonatite genesis and eruptive behavior. Earth Planet. Sci. Lett. 361, 379–390. doi:10.1016/j.epsl.2012.11.006

Fedortchouk, Y., Canil, D., Carlson, J.A., 2002. Intensive Variables in Primary Kimberlite Magmas (Lac de Gras, N.W.T., Canada) and Application for Diamond Preservation. AGU Fall Meet. Abstr. -1, 1348.

Ghosh, S., Ohtani, E., Litasov, K.D., Terasaki, H., 2009. Solidus of carbonated peridotite from 10 to 20 GPa and origin of magnesiocarbonatite melt in the Earth's deep mantle. Chem. Geol., Volatiles and Volatile-Bearing Melts in the Earth's Interior 262, 17–28. doi:10.1016/j.chemgeo.2008.12.030

Gudfinnsson, G.H., Presnall, D.C., 2005. Continuous Gradations among Primary Carbonatitic, Kimberlitic, Melilititic, Basaltic, Picritic, and Komatiitic Melts in Equilibrium with Garnet Lherzolite at 3–8 GPa. J. Petrol. 46, 1645–1659. doi:10.1093/petrology/egi029

Guillot, B., Sator, N., 2011. Carbon dioxide in silicate melts: A molecular dynamics simulation study. Geochim. Cosmochim. Acta 75, 1829–1857. doi:10.1016/j.gca.2011.01.004

Hawthorne, J.B., 1975. Model of a kimberlite pipe. Phys. Chem. Earth 9, 1–15. doi:10.1016/0079-1946(75)90002-6

Iacono-Marziano, G., Morizet, Y., Le Trong, E., Gaillard, F., 2012. New experimental data and semi-empirical parameterization of H2O–CO2 solubility in mafic melts. Geochim. Cosmochim. Acta 97, 1–23. doi:10.1016/j.gca.2012.08.035

Janse, A.J.A., 1975. Kimberlite and related rocks from the Nama Plateau of South-West Africa. Phys. Chem. Earth 9, 81–94. doi:10.1016/0079-1946(75)90009-9

Kavanagh, J.L., Sparks, R.S.J., 2009. Temperature changes in ascending kimberlite magma. Earth Planet. Sci. Lett. 286, 404–413. doi:10.1016/j.epsl.2009.07.011

Keppler, H., 2003. Water solubility in carbonatite melts. Am. Mineral. 88, 1822–1824.

Kervyn, M., Ernst, G.G.J., Klaudius, J., Keller, J., Kervyn, F., Mattsson, H.B., Belton, F., Mbede, E., Jacobs, P., 2008. Voluminous lava flows at Oldoinyo Lengai in 2006: chronology of events and insights into the shallow magmatic system. Bull. Volcanol. 70, 1069–1086. doi:10.1007/s00445-007-0190-x

Kopylova, M.G., Matveev, S., Raudsepp, M., 2007. Searching for parental kimberlite melt. Geochim. Cosmochim. Acta 71, 3616–3629. doi:10.1016/j.gca.2007.05.009

Larsen, L.M., Rex, D.C., 1992. A review of the 2500 Ma span of alkaline-ultramafic, potassic and carbonatitic magmatism in West Greenland. Lithos 28, 367–402. doi:10.1016/0024-4937(92)90015-Q

Mattey, D.P., 1991. Carbon dioxide solubility and carbon isotope fractionation in basaltic melt. Geochim. Cosmochim. Acta 55, 3467–3473. doi:10.1016/0016-7037(91)90508-3

449 Mercier, M., Di Muro, A., Giordano, D., Métrich, N., Lesne, P., Pichavant, M., Scaillet, B.,
450 Clocchiatti, R., Montagnac, G., 2009. Influence of glass polymerisation and oxidation
451 on micro-Raman water analysis in alumino-silicate glasses. Geochim. Cosmochim.
452 Acta 73, 197–217. doi:10.1016/j.gca.2008.09.030
453 Mitchell, R.H., 1986. kimberlites mineralogy geochemistry and petrology. Plenum, NY.
454 Mitchell, R.H., 2005. Carbonatites and Carbonatites and Carbonatites. Can. Mineral. 43,
455 2049–2068. doi:10.2113/gscanmin.43.6.2049
456 Mitchell, R.H., 2008. Petrology of hypabyssal kimberlites: Relevance to primary magma
457 compositions. J. Volcanol. Geotherm. Res. 174, 1–8.
458 doi:10.1016/j.jvolgeores.2007.12.024
459 Morizet, Y., Brooker, R.A., Iacono-Marziano, G., Kjarsgaard, B.A., 2013. Quantification of
460 dissolved CO2 in silicate glasses using micro-Raman spectroscopy. Am. Mineral. 98,
461 1788–1802. doi:10.2138/am.2013.4516
462 Morizet, Y., Brooker, R.A., Kohn, S.C., 2002. CO2 in haplo-phonolite melt: solubility,
463 speciation and carbonate complexation. Geochim. Cosmochim. Acta 66, 1809–1820.
464 doi:10.1016/S0016-7037(01)00893-6
465 Morizet, Y., Paris, M., Gaillard, F., Scaillet, B., 2014. Carbon dioxide in silica-undersaturated
466 melt Part I: The effect of mixed alkalis (K and Na) on CO2 solubility and speciation.
467 Geochim. Cosmochim. Acta.
468 Nelson, D.R., Chivas, A.R., Chappell, B.W., McCulloch, M.T., 1988. Geochemical and
469 isotopic systematics in carbonatites and implications for the evolution of ocean-island
470 sources. Geochim. Cosmochim. Acta 52, 1–17. doi:10.1016/0016-7037(88)90051-8
471 Papale, P., Moretti, R., Barbato, D., 2006. The compositional dependence of the saturation
472 surface of H2O+CO2 fluids in silicate melts. Chem. Geol. 229, 78–95.
473 doi:10.1016/j.chemgeo.2006.01.013
474 Pawley, A.R., Holloway, J.R., McMillan, P.F., 1992. The effect of oxygen fugacity on the
475 solubility of carbon-oxygen fluids in basaltic melt. Earth Planet. Sci. Lett. 110, 213–
476 225. doi:10.1016/0012-821X(92)90049-2
477 Peccerillo, A., Poli, G., Serri, G., 1988. Petrogenesis of orenditic and kamafugitic rocks from
478 central Italy. Can. Mineral. 26, 45–65.
479 Price, S.E., Russell, J.K., Kopylova, M.G., 2000. Primitive Magma From the Jericho Pipe,
480 N.W.T., Canada: Constraints on Primary Kimberlite Melt Chemistry. J. Petrol. 41,
481 789–808. doi:10.1093/petrology/41.6.789
482 Rohrbach, A., Schmidt, M.W., 2011. Redox freezing and melting in the Earth/'s deep mantle
483 resulting from carbon-iron redox coupling. Nature 472, 209–212.
484 doi:10.1038/nature09899
485 Russell, J.K., Porritt, L.A., Lavallée, Y., Dingwell, D.B., 2012. Kimberlite ascent by
486 assimilation-fuelled buoyancy. Nature 481, 352–356. doi:10.1038/nature10740
487 Shishkina, T.A., Botcharnikov, R.E., Holtz, F., Almeev, R.R., Portnyagin, M.V., 2010.
488 Solubility of H2O- and CO2-bearing fluids in tholeiitic basalts at pressures up to
489 500 MPa. Chem. Geol. 277, 115–125. doi:10.1016/j.chemgeo.2010.07.014
490 Sparks, R.S.J., Brooker, R.A., Field, M., Kavanagh, J., Schumacher, J.C., Walter, M.J.,
491 White, J., 2009. The nature of erupting kimberlite melts. Lithos 112, Supplement 1,
492 429–438. doi:10.1016/j.lithos.2009.05.032
493 Stolper, E., Holloway, J.R., 1988. Experimental determination of the solubility of carbon
494 dioxide in molten basalt at low pressure. Earth Planet. Sci. Lett. 87, 397–408.
495 doi:10.1016/0012-821X(88)90004-0
496 White, S.H., de Boorder, H., Smith, C.B., 1995. Structural controls of kimberlite and
497 lamproite emplacement. J. Geochem. Explor. 53, 245–264. doi:10.1016/0375-
498 6742(94)00033-8

Wyllie, P.J., 1989. Origin of carbonatites; evidence from phase equilibrium studies. Unwin Hyman : London, United Kingdom, United Kingdom, pp. 500–545.

TABLES

Table 1: Starting oxide and natural rock powder mix compositions. The composition of a natural lamproite from Torre Alfina, Italy, (Peccerillo et al., 1998), fused twice at 1400°C and used to prepare the oxide-mix compositions is reported at the top of the table.

Table 2: Run conditions, EMPA analyses (averaged from 20), H_2O determined by elemental analyser (Flash) and CO_2 determined from: (i) EMPA (by subtracting H_2O content to EMPA shortfall), (ii) Elemental analyser (Flash), (iii) Micro-Raman spectroscopy (following the method of Morizet et al., (2013) and (iv) Weight loss measured by puncturing the capsule (allowing the CO_2 to escape) after each run. Run duration was of 2 hours in all experiments.

Table 3: Adjusted parameters (and corresponding standard error on multiple non-linear regression fit) to calculate CO_2 solubility from Eq. (1)

FIGURES

Figure 1: Optical microphotograph showing the results from various supra-liquidus experimental run producing a pure glass in all cases excepted for sample TA6_1_5 (lower right) in which quench crystals give a “milky” aspect to the otherwise glassy product. All samples shown are synthesised in IHPV apparatus excepted sample TA6_1_5 which was synthesised with piston cylinder. Corresponding SEM images are shown in Fig S1.

Figure 2: CO_2 solubility measurements for a series of compositions across the silicate to carbonate melt transitions equilibrated at 350 MPa. The SiO_2+Al_2O_3 content is reported including volatiles. For most experiments, CO_2 content is estimated from elemental analyser and associated error is estimated at ± 1 wt%. CO_2 content from Iacono-Marziano et al., (2012) is estimated from FTIR analyses.

Figure 3:CO_2 solubility as a function of pressure for three Kimberlite/Transitional and two silicate melt compositions spanning SiO_2 content of 18 to 41 wt% and SiO_2 + Al_2O_3 content of 21 to 51 wt% respectively (calculated including volatiles and corresponding to SiO_2 + Al_2O_3 contents of 27 to 54 wt% on a volatile-free basis). The light-brown to green colour part of the plot represents the upper 3 km of crust, corresponding to the typical "root zone" of Kimberlites. Dashed lines are fitted by eye through the data points.

Figure 4: Modelled evolution of CO_2 solubility as a function of pressure using equation (1) for melt compositions ranging from 0 to 41 wt% SiO_2 and 0 to 51 wt% SiO_2 + Al_2O_3. Experiments of corresponding chemistry are shown as squares of matching colour.

Figure 5: CO_2 solubility measurements from this study and the literature for compositions across the silicate to carbonate melt transition, equilibrated at 2000, 1500, 350, 200, 100 and 50 MPa. Literature data are from Brooker and Kjarsgaard, 2011; Brooker et al., 2011; Iacono-Marziano et al., 2012; Brooker et al., 2001; Brooker 1995; Morizet et al., 2013 Morizet et al., 2014 and Brey and Ryabchikov, 1994. Note that literature data are reported using the experiment total pressure and not the P_{CO2}. Model prediction values from equation (1) are shown for a range of pressure (2000 to 20 MPa) as dotted black curves.

548 **Figure 6**: Experimentally determined vs. calculated CO_2 solubility using equation (1). Doted
549 red line represent the 1:1 line while continuous red lines on either sides represent the ± 2σ
550 deviation.
551

552 ## SUPPLEMENTARY INFORMATION

553 **TableS1:** Standard deviation for EMP analyses reported in Table 2 (n=20).
554

555 **Table S2**: Run conditions, EMPA analyses and CO_2 determined from Raman or by bulk CO_2
556 LECO analyser for experiments from Brooker et al., (2011); Brooker and Kjarsgaard, (2011);
557 Iacono-Marziano et al., (2012); Brooker (1995) and Morizet et al., (2014).
558

559 **Figure S1:** Scanning electron microscopy (SEM) images of experimental charges shown in
560 Fig. 1. All run produced a pure glass, excepted sample TA6_1_5 (lower right) in which
561 quench crystals are pervasive.
562

563 **Figure S2:**Comparison between CO_2 content in experimental charges determined by (i)
564 EMPA (by subtracting H_2O content to EMPA shortfall), (ii) Elemental analyser (Flash), (iii)
565 Micro-Raman spectroscopy (following the method of Morizet et al., 2013), (iv) Weight loss
566 measured by puncturing the capsule (allowing the CO_2 to escape) after each run and (v)
567 EMPA shortfall without correction.
568

Name	SiO_2	TiO_2	Al_2O_3	FeO	MgO	CaO	Na_2O	K_2O	P_2O_5	CO_2	Total
TA	55.74	1.34	13.05	5.83	9.43	5.45	0.96	7.68	0.51	0.00	100
TA15	11.01	0.09	2.34	0.41	8.45	36.36	0.27	2.14	0.04	38.90	100
TA6	16.60	0.20	3.85	0.86	6.93	35.48	0.28	2.27	0.07	33.47	100
TA7	20.08	0.25	4.66	1.08	8.16	32.50	0.34	2.74	0.10	30.09	100
TA8	21.66	0.30	5.03	1.30	8.21	31.30	0.37	2.96	0.11	28.75	100
TA9	23.11	0.34	5.37	1.49	8.26	30.20	0.40	3.16	0.13	27.53	100
TA10	23.79	0.36	5.53	1.58	8.29	29.68	0.41	3.26	0.14	26.95	100
TA11	30.18	0.56	7.04	2.43	8.52	24.84	0.52	4.14	0.21	21.56	100
TA12	37.70	0.79	8.81	3.43	8.78	19.14	0.65	5.18	0.30	15.22	100

Table 1: Starting oxide and natural rock powder mix compositions. The composition of a natural lamproite from Torre Alfina, Italy, (Peccerillo et al., 1998), fused twice at 1400°C and used to prepare the oxide-mix compositions is reported at the top of the table.

Experiment	Pressure (MPa)	Temperature (°C)	SiO_2	TiO_2	Al_2O_3	FeO	MnO	MgO	CaO	Na_2O	K_2O	P_2O_5	Total	Shortfall	H_2O (Flash)	CO_2 (EMPA)	CO_2 (Flash)	CO_2 (Raman)	CO_2 (weight loss)
TA6_1_1	357.2	1225	18.44	0.2	2.05	0.74	0.03	6.87	45.25	0.3	2.3	0.04	76.22	23.8	1.54	22.24	21.84	21.4	24.4
TA6_1_4	178	1220-1260	17.97	0.19	2.63	0.81	0.04	6.75	44.8	0.41	2.19	0.04	75.83	24.2	1.19	22.98	20.07	23.4	18.9
TA7_1_1	340.2	1190	23.58	0.29	4.27	1.12	0.03	9.91	37.22	0.3	3.26	0.07	80.07	19.9	1.09	18.84	16.28	18.2	nd
TA9_1_1	336.4	1225	26.07	0.35	5.7	1.49	0.04	8.18	36.87	0.45	3.28	0.09	82.52	17.5	1.57	15.91	14.95	14.7	13.4
TA10_1_1	336.4	1225	26.77	0.35	5.8	1.64	0.05	8.52	36.24	0.4	3.39	0.09	83.25	16.8	1.73	15.02	13.80	14.4	12.0
TA11_1_1	347.8	1225	34.48	0.6	7.81	2.85	0.06	10	29.05	0.66	4.42	0.12	90.04	10.0	0.99	8.97	7.50	4.7	7.8
TA12_1_1	347.8	1225	40.97	0.82	9.74	3.68	0.06	9.38	22.96	0.82	5.58	0.19	94.19	5.8	0.59	5.22	2.79	3.5	3.7
TA6_1_5	1500	1300	*Crystallised*												1.36		24.85		nd
TA6_1_6	59.3	1225	*Crystallised*												0.84		15.87		12.7
TA7_1_2	179.2	1225	21.50	0.30	4.00	1.20	0.10	8.00	39.70	0.40	4.30	0.10	79.60	20.40	0.77	19.63	16.36	13.3	15.3
TA7_1_3	48.9	1215-1290	*Crystallised*												0.54		12.86		9.1
TA6_2_1	105.4	1270	17.80	0.20	2.40	0.70	0.10	8.10	45.20	0.20	2.50	0.10	77.20	22.80	0.79	22.01	16.47	16.3	18.3
TA7_1_4	100.7	1225	20.40	0.40	3.00	1.20	0.00	7.10	43.30	0.50	3.80	0.10	79.80	20.20	0.76	19.44	15.09	17.1	13.0
TA9_1_2	100.7	1225	24.50	0.50	4.40	1.90	0.00	8.10	39.80	0.50	4.20	0.10	84.20	15.80	0.59	15.22	10.12	10.8	11.0
TA15_1_1	351	1225	*Crystallised*												1.60		28.63		31.4
TA10_1_2	101	1225	*Crystallised*												0.71		9.00	10.18	8.59
TA11_1_2	101	1225	34.68	0.96	9.87	3.95	0.05	8.20	26.50	0.67	6.31	0.22	91.42	8.58	0.50	8.08	2.58	2.37	2.09
TA12_1_3	101	1225	43.16	0.85	9.82	3.80	0.06	9.85	22.09	0.96	5.74	0.23	96.57	3.43	0.56	2.87	1.02	1.35	1.55

Table 2: Run conditions, EMP analyses (averaged from 20), H_2O determined by elemental analyser (Flash) and CO_2 determined from: (i) EMPA (by subtracting H_2O content to EMPA shortfall), (ii) Elemental analyser (Flash), (iii) Micro-Raman spectroscopy (following the method of Morizet *et al.*, 2013) and (iv) Weight loss measured by puncturing the capsule (allowing the CO_2 to escape) after each run . Run duration was of 2 hours in all experiments.

	a	b	c	d	e	f	D
Value	-0.001271	-0.476116	0.132494	-0.322187	-4.501117	-0.163249	50
Std. Err.	0.000244	0.040612	0.016065	0.020635	0.281876	0.008332	1.4

Table 3: Adjusted parameters (and corresponding standard error on multiple non-linear regression fit) to calculate CO_2 solubility from Eq. (1). Regression was calculated from over 160 data points (detail in text).

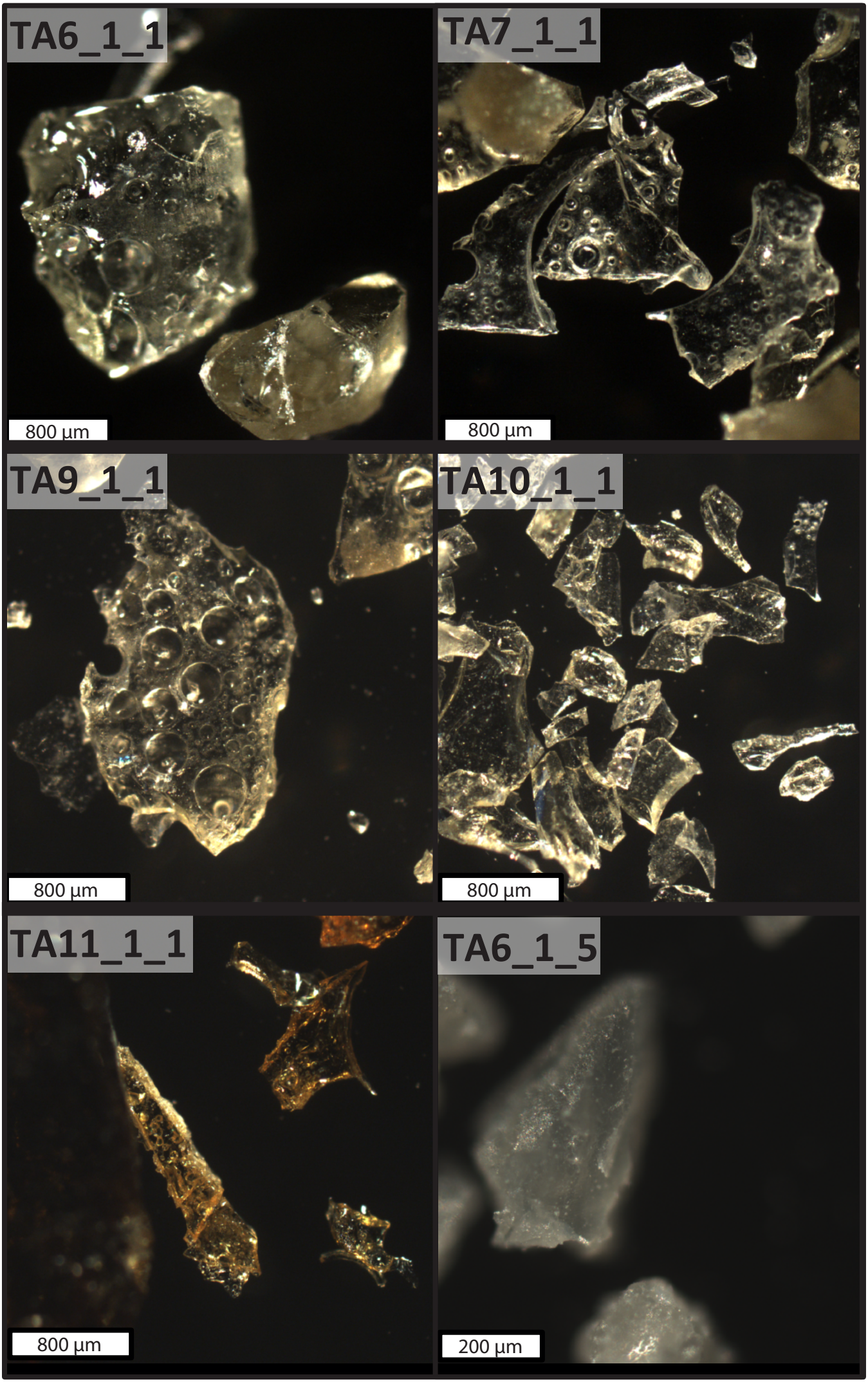

Figure 1. Moussallam et al.

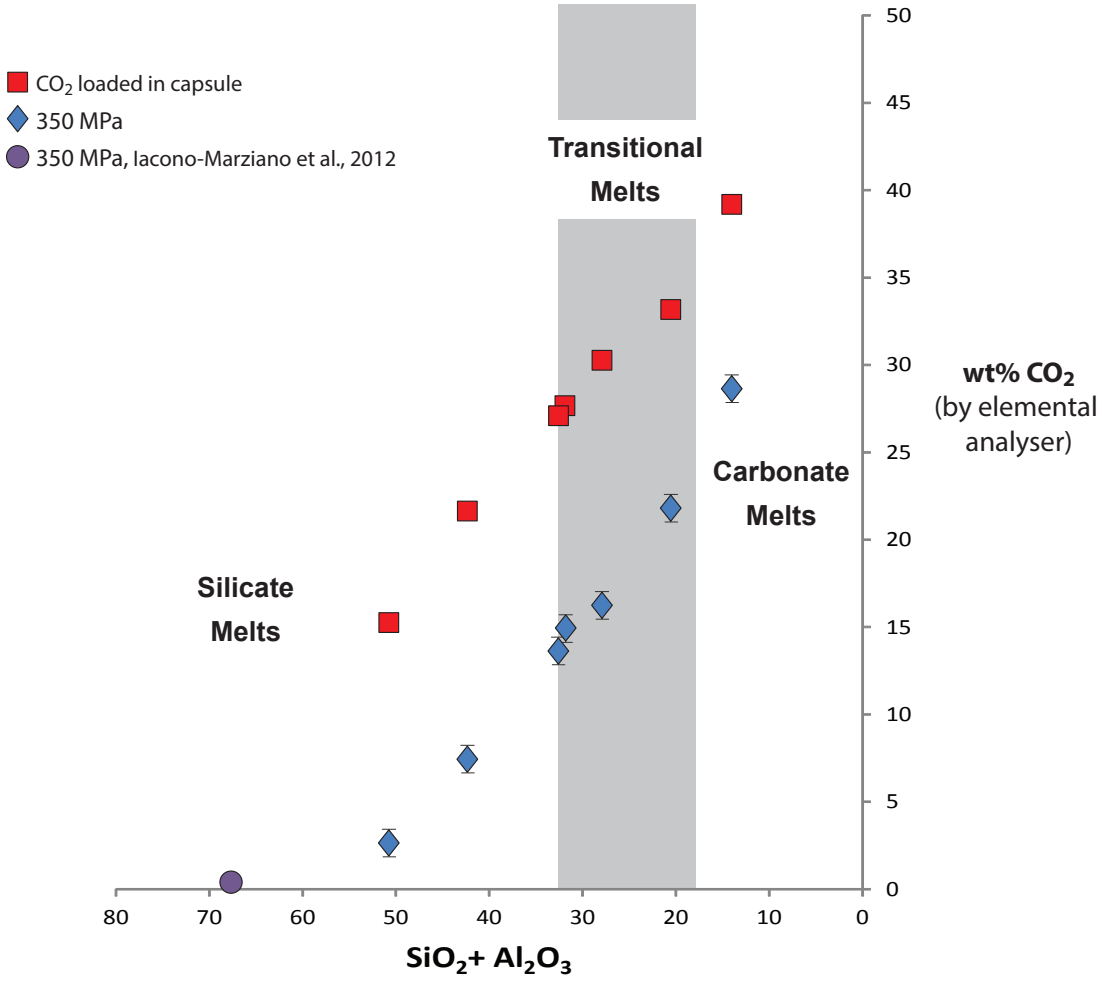

Figure 2, Moussallam et al.

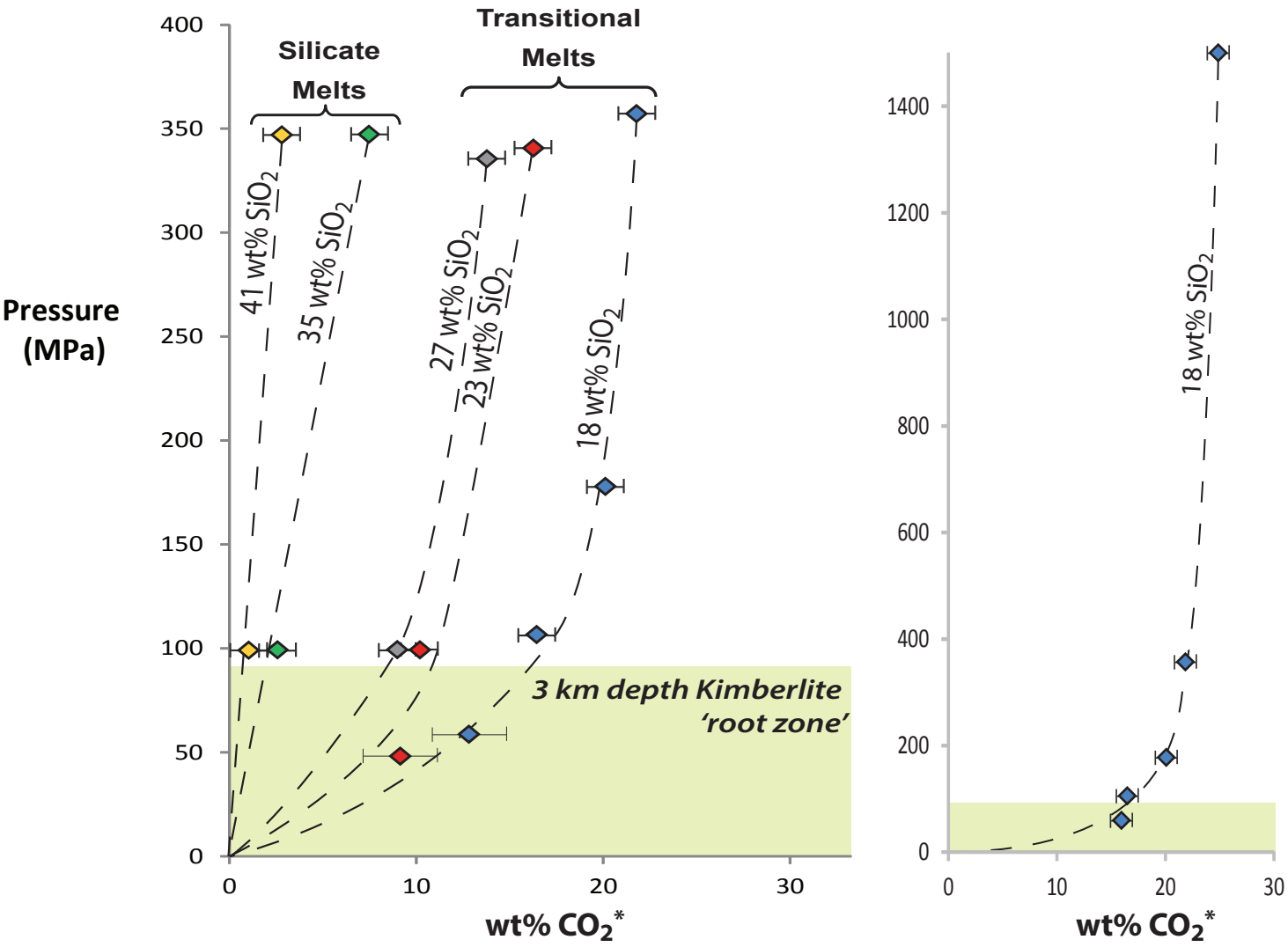

*(by elemental analyser and weight loss)

Figure 3, Moussallam et al.

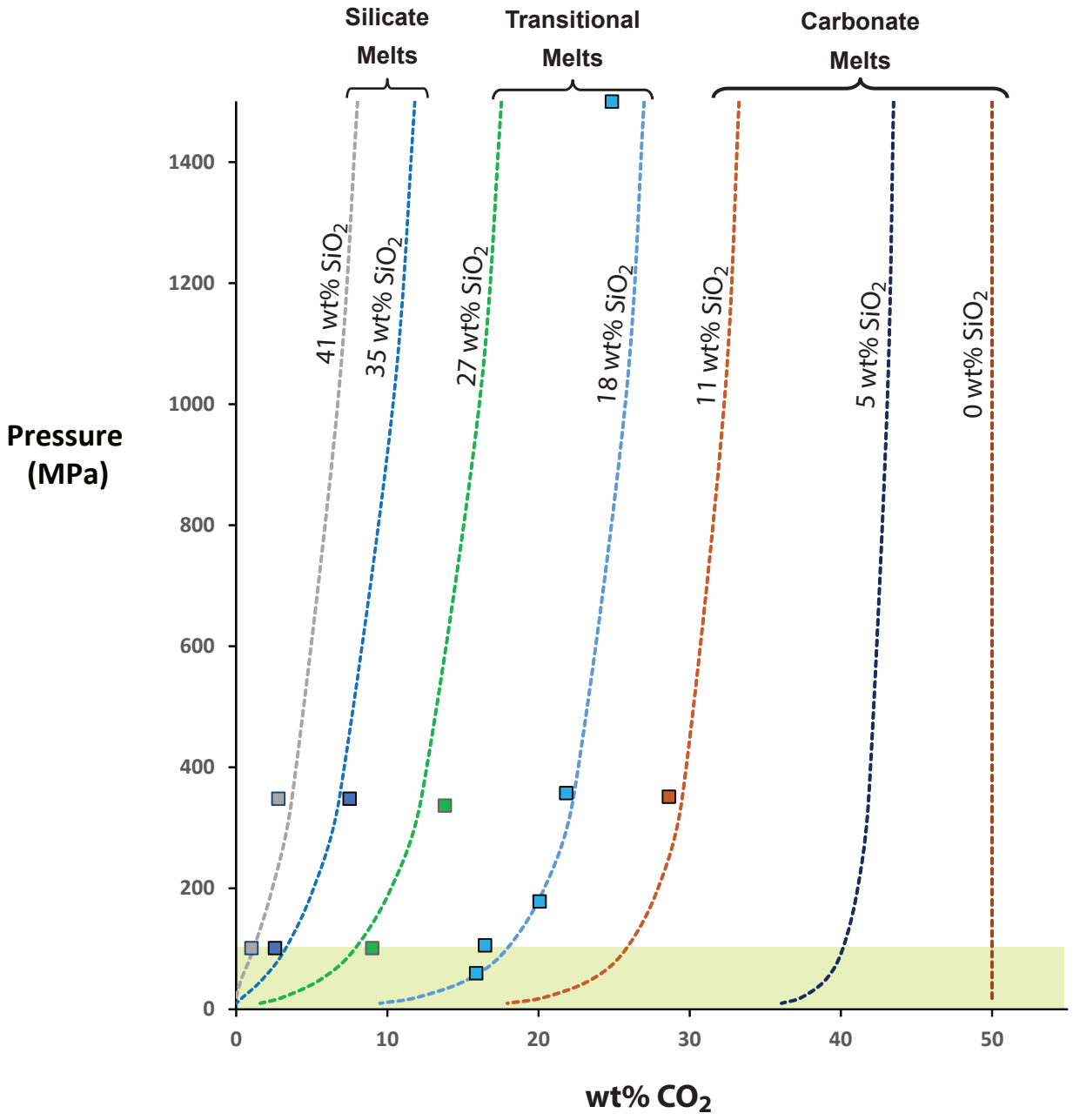

Figure 4, Moussallam et al.

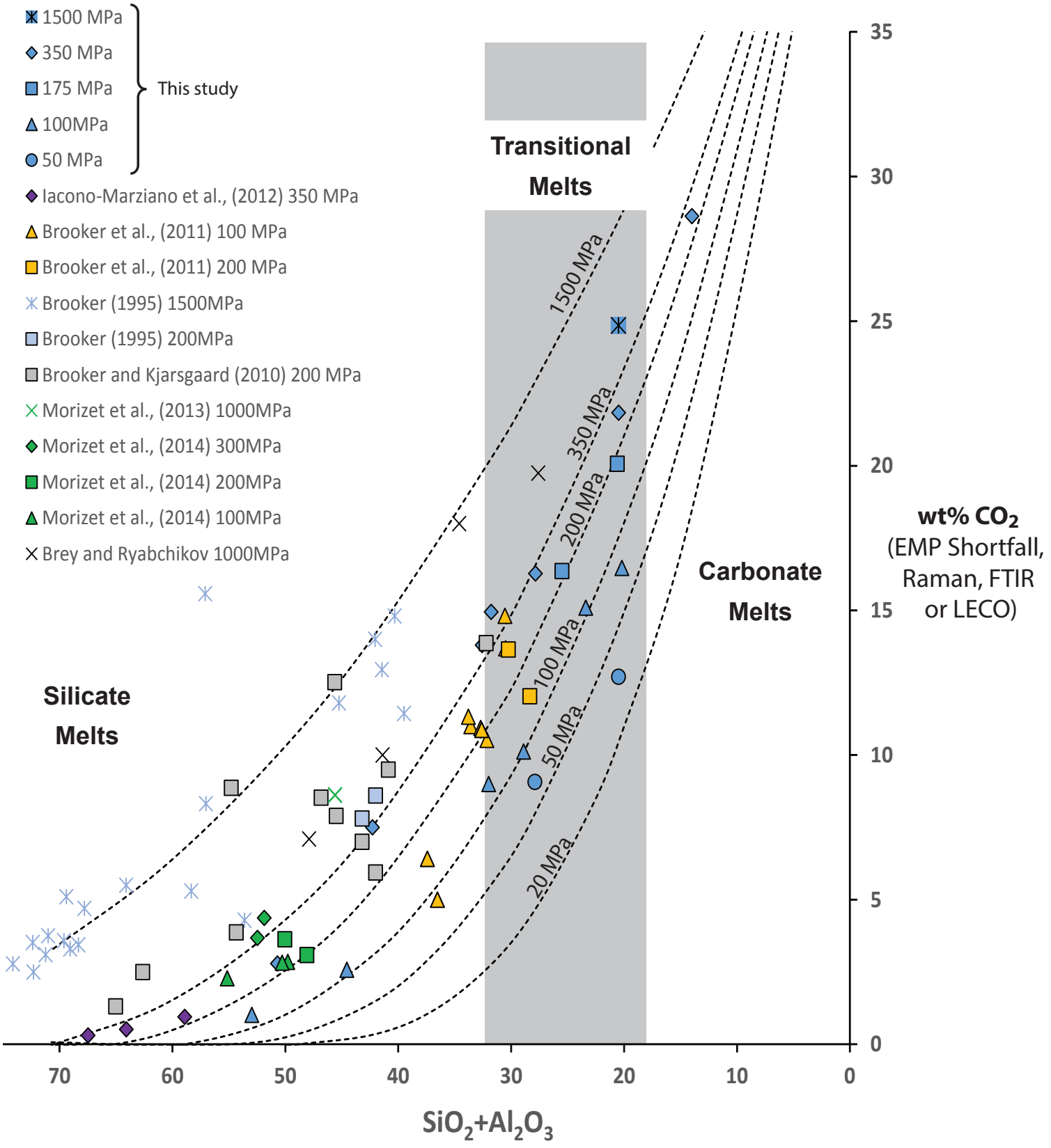

Figure 5, Moussallam et al.

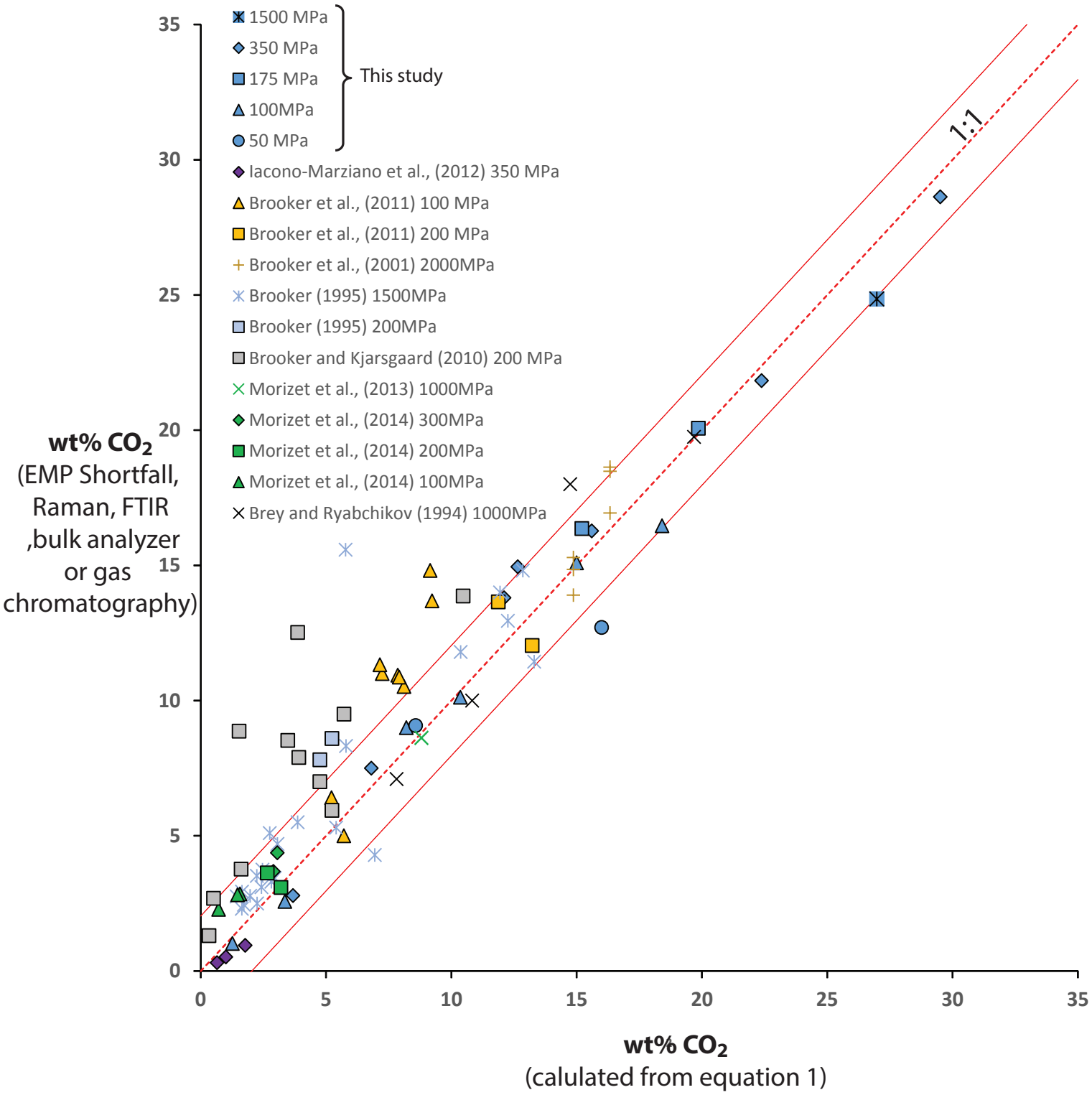

Figure 6, Moussallam et al.

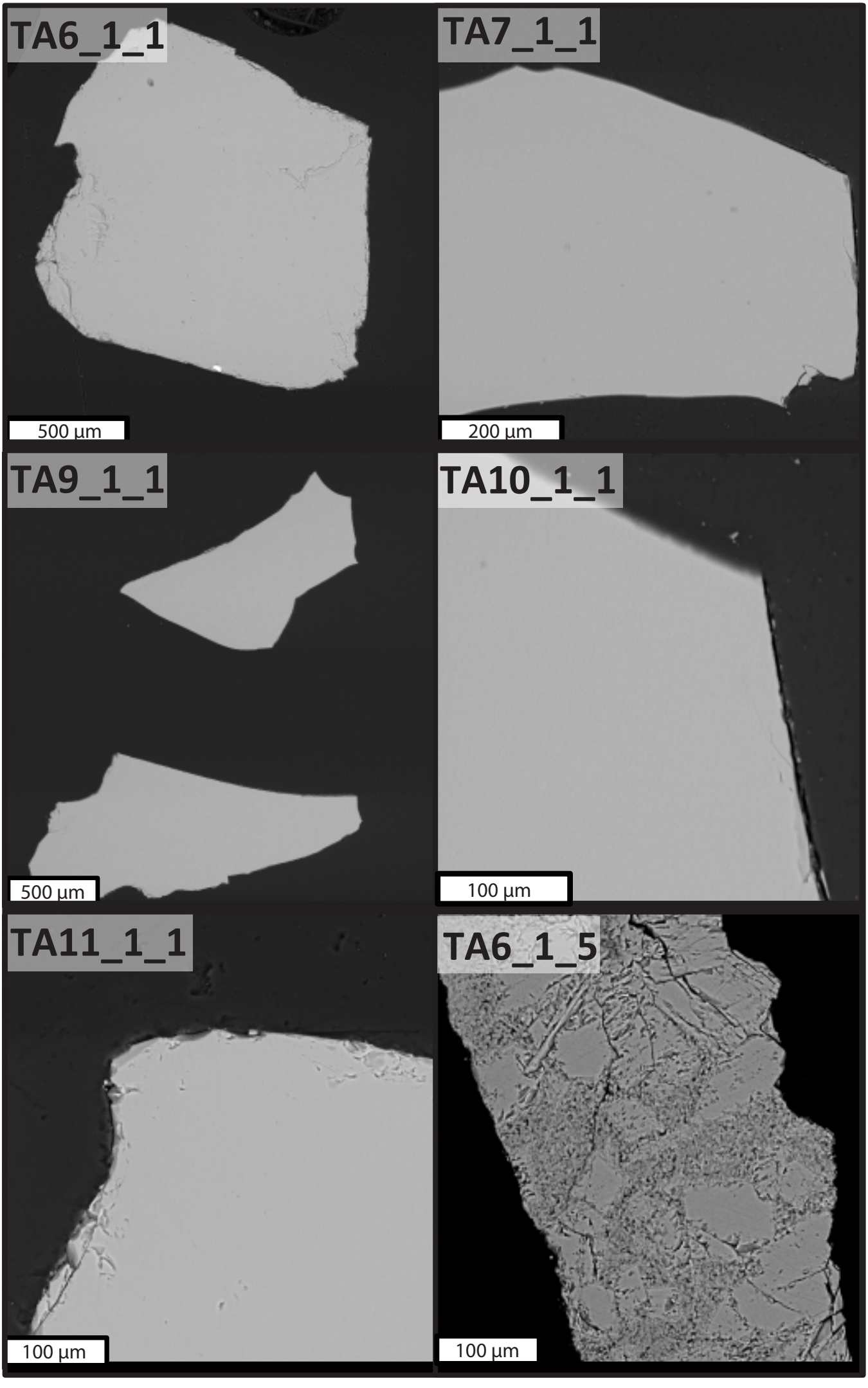

Figure S1. Moussallam et al.

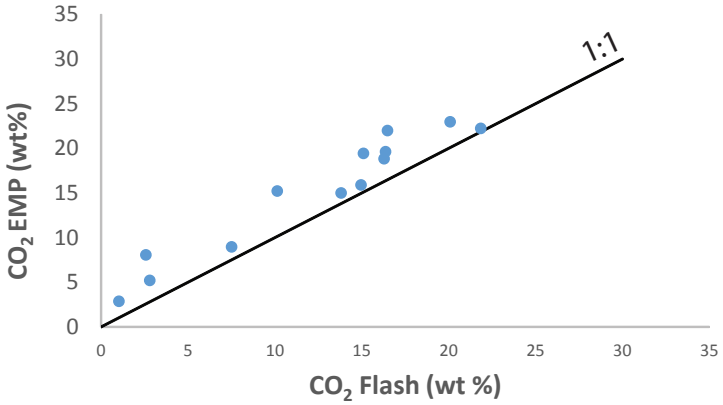

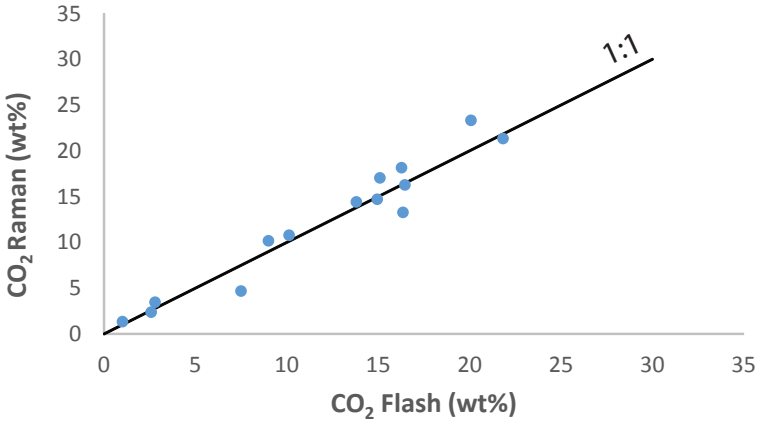

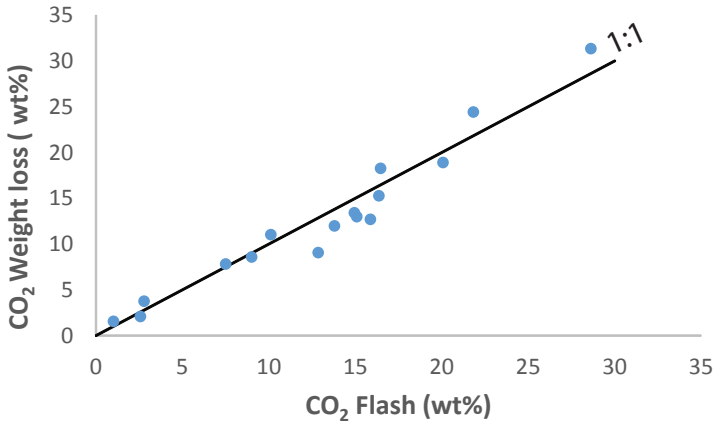

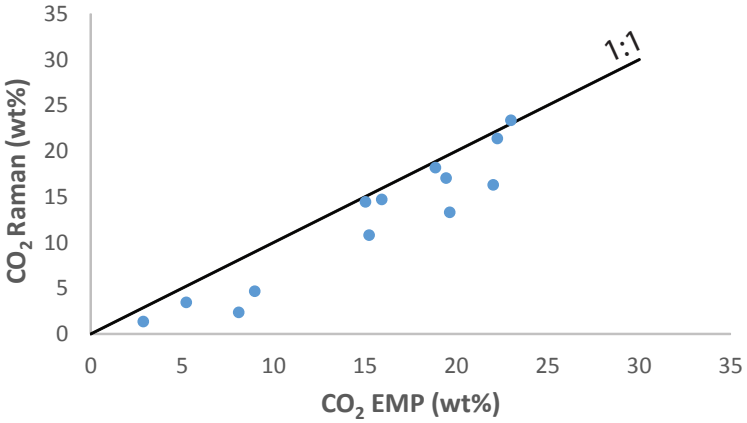

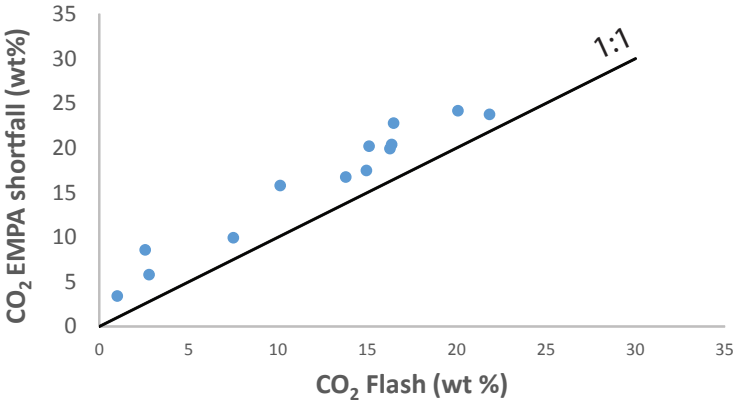

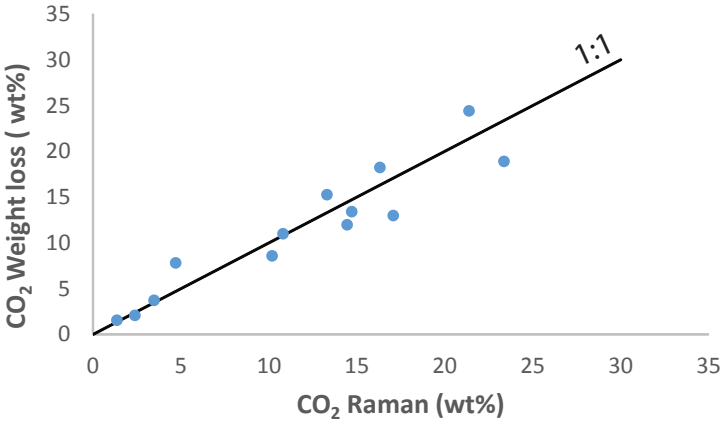

Figure S2, Moussallam et al.